Chinese Physics Letters

LETTER

Quasi-Periodic Moiré Patterns and Dimensional Localizations in Twisted Three-Dimensional Optical Lattices

Cite as: Ce Wang *et al*. 2026 *Chin. Phys. Lett.* **43** 090302

DOI CSTR

Recommended Articles

Visualizing the Local Twist Angle Variation within and between Domains of Twisted Bilayer Graphene
Jiawei Hu, Shiyu Zhu, Qianying Hu, Yunhao Wang, Chengmin Shen, Haitao Yang, Xiaoshan Zhu, Qing Huan, Yang Xu, and Hong-Jun Gao
Chin. Phys. Lett. **41**, (2024)

Nano-Opto-Electro-Mechanical Systems from Moiré Superlattices
Qin-Yang Zeng, Gui-Xin Su, Xin-Yu Mei, Han Wang, Ping-Heng Tan, and Xin Zhang
Chin. Phys. Lett. **43**, 050701 (2026)

Thermal Entropy, Density Disorder, and Antiferromagnetism of Repulsive Fermions in 3D Optical Lattice
Yu-Feng Song, Youjin Deng, and Yuan-Yao He
Chin. Phys. Lett. **42**, 110710 (2025)

Vortex Solitons in Atomic–Molecular Bose–Einstein Condensates with a Square-Optical-Lattice Potential
Yuan Zhao, Wan Liu, Linjia Wang, Zhuo Fan, Qin Zhou, Boris A. Malomed, Shunfang Chen, and Siliu Xu
Chin. Phys. Lett. **42**, 090002 (2025)

Remote Comparison of Two Sr Optical Lattice Clocks through a 58 km Fiber Link
Tang-Yin Liao *et al*.
Chin. Phys. Lett. **42**, 034201 (2025)

Interference Pattern of Floquet Modes in Frequency Space
Du-Yi Ou-Yang, Yan-Hua Zhou, Ya Zhang, Xiao-Tong Lu, Hong Chang, Tao Wang, and Xue-Feng Zhang
Chin. Phys. Lett. **42**, 060601 (2025)

A series journal of Chinese Physical Society distributed by IOP Publishing

Chinese Physics Letters

Chin. Phys. Lett. **43** 090302 (2026)

LETTER

DOI: 10.1088/0256-307X/43/9/090302
CSTR: 32039.14.0256-307X.43.9.090302

Quasi-Periodic Moiré Patterns and Dimensional Localizations in Twisted Three-Dimensional Optical Lattices

Ce Wang[1], Chao Gao[2,3,*], and Zhe-Yu Shi[4,*]

[1]School of Physics Science and Engineering, Tongji University, Shanghai 200092, China
[2]Department of Physics, Zhejiang Normal University, Jinhua 321004, China
[3]Zhejiang Institute of Photoelectronics, Jinhua 321004, China
[4]State Key Laboratory of Precision Spectroscopy, Institute of Quantum Science and Precision Measurement, School of Physics, East China Normal University, Shanghai 200062, China

[*]Corresponding authors. Email: gaochao@zjnu.edu.cn; zyshi@lps.ecnu.edu.cn

Recent advances in spin-dependent optical lattices [Meng *et al.* 2023 Nature 615, 231] have enabled the experimental implementation of two superimposed three-dimensional lattices, presenting new opportunities to investigate three-dimensional moiré physics in ultracold atomic gases. This work studies the moiré physics of atoms within a spin-dependent cubic lattice with relative twists along different directions. It is discovered that dimensionality significantly influences the low-energy moiré physics. From a geometric perspective, this manifests in the observation that moiré patterns, generated by rotating lattices along different axes, can exhibit either periodic or quasi-periodic behavior—a feature not present in two-dimensional systems. We develop a low-energy effective theory applicable to systems with arbitrary rotation axes and small rotation angles. This theory elucidates the emergence of quasi-periodicity in three dimensions and demonstrates its correlation with the arithmetic properties of the rotation axes. Numerical analyses reveal that these quasi-periodic moiré potentials can lead to distinctive dimensional localization behaviors of atoms, manifesting as localized wave functions in planar or linear configurations.

When two identical two-dimensional (2D) lattices are overlaid with a slight twist, periodic interference patterns known as moiré patterns emerge at the macroscopic scale. These patterns have garnered significant attention, as recent studies of twisted double-layered 2D materials demonstrate that moiré patterns can significantly alter systems' electronic properties. Remarkable phenomena have been discovered in 2D moiré systems, including flat bands [1−3], unconventional superconductivity [4−7], and fractional quantum anomalous Hall effect [8−11].

While moiré patterns are predominantly observed in solid-state materials, they can be engineered in various synthetic structures, including photonic crystals [12−17], phononic crystals [18−22], lattice nanocavities [23−25], and optical lattices [26−35]. These structures provide versatile platforms for exploring moiré physics that are challenging to study in conventional condensed matter systems. Notably, recent experimental advances in synthetic moiré superlattices have demonstrated interesting moiré physics for bosonic matters, particularly the localization of electromagnetic waves [13,36] and novel superfluid to Mott insulator transitions of bosonic atoms [29]. We have also proposed that through an extension of the current twisted bilayer optical lattice configuration, it is possible to implement a twisted three-dimensional (3D) optical lattice for ultracold atomic gases [37]. This offers a unique opportunity for the study of 3D moiré physics, providing insights previously inaccessible through conventional condensed matter materials.

Building upon our previous work [37], which establishes the complete classification for 3D moiré crystals, i.e., lattices with commensurate twists, this research explores incommensurate twist configurations, termed quasi-moiré crystals. Specifically, we focus on moiré physics in twisted cubic lattices with small twist angles and probe the role of dimensionality on moiré physics.

Before entering into any detailed analysis, we shall first clarify the convention used throughout this work and provide some geometric intuitions that highlight the significance of dimensionality. Here, the term "moiré pattern" refers specifically to the long-wavelength pattern obtained at the lowest order in the small angular deviation from a commensurate rotation. This should be distinguished from the exact superposition of two lattices, which in 2D can be periodic, quasi-periodic, or generally aperiodic depending on the matching condition and rotation angle [13,24,38]. The key differentiation between moiré physics in two and three dimensions stems from the distinctive parameterization of rotations. In 2D systems, the rotation is characterized by a single parameter, i.e., the twist angle θ. The two resulting moiré reciprocal vectors are obtained from the reciprocal basis vectors of the underlying lattice through a common scaling and rotation and therefore generate a 2D Bravais lattice. Consequently, the structure of the moiré pattern is uniquely determined by the underlying lattice, resulting in periodic patterns. Adjusting the twist angle simply scales the whole pattern by a dimensionless factor. This emergent periodicity also permits one to define a moiré Brillouin zone and moiré bands within the small-angle continuum theory, irrespective of whether the two microscopic lattices are exactly commensurate [1]. In contrast, a 3D rotation is determined by both the twist angle $\theta \in [0,\pi)$ and the rotation axis $\boldsymbol{L} \in \mathbb{R}^3$. The three resulting moiré reciprocal vectors lie in the plane perpendicular to $\boldsymbol{L}$ but do not necessarily generate a 2D Bravais lattice. The parameterization enables the generation of more diverse moiré patterns from a single 3D lattice. In Fig. 1, we plot the moiré patterns of twisted cubic lattices with various rotation axes $\boldsymbol{L}$ by projecting lattice points onto 2D planes perpendicular to it. The resulting patterns exhibit remarkable diversity, manifesting as periodic [Fig. 1(a)], quasi-periodic [Fig. 1(c)], or hybrid structures that display periodicity along one direction while maintaining quasi-periodicity along the others [Fig. 1(b)].

This work addresses two central questions regarding 3D quasi-

Received 24 June 2026; accepted 14 August 2026; published 17 September 2026
© 2026 Chinese Physical Society and IOP Publishing Ltd. All rights, including for text and data mining, AI training, and similar technologies, are reserved.

Check for updates

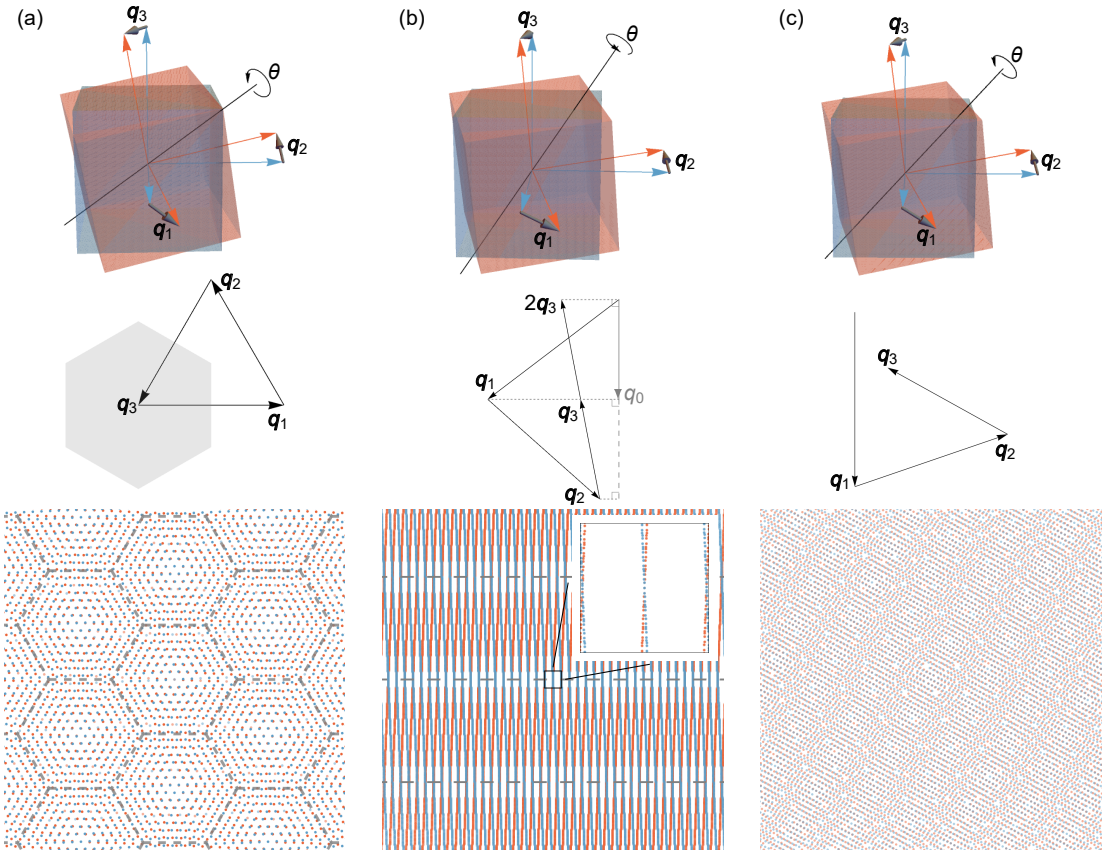

Fig. 1. Schematic plot of the moiré primitive vectors $\boldsymbol{q}_i$ and the moiré patterns for twisted cubic lattices with rotation axes $\boldsymbol{L} = (1, 1, 1)$ [column (a), periodic scenario], $\boldsymbol{L} = (1, \varphi, \varphi^2)$ [column (b), the golden axis, hybrid scenario], and $\boldsymbol{L} = (1, \sqrt{\varphi}, \varphi)$ [column (c), the Kepler axis, ergodic scenario]. Here $\varphi = (\sqrt{5}+1)/2$ is the golden ratio. The first row illustrates the moiré primitive vectors $\boldsymbol{q}_i$ in 3D momentum space. The blue (red) cubes represent the first Brillouin zones of the underlying A (B) sublattices. The middle row illustrates the relations between moiré primitive vectors by plotting them on the plane perpendicular to $\boldsymbol{L}$. The gray area in (a) and the line segment in (b) mark the period of $S_{\boldsymbol{q}} \equiv \{n_1\boldsymbol{q}_1 + n_2\boldsymbol{q}_2 + n_3\boldsymbol{q}_3\}$. The last row displays the corresponding moiré patterns. Each diagram is generated by projecting 2×41^3 lattice points onto the plane perpendicular to the rotation axis $\boldsymbol{L}$. The dashed lines mark the periodicity calculated using the moiré primitive vectors $\boldsymbol{q}_i$. One can see that the moiré pattern of a quasi-moiré crystal can be either 2D periodic [panel (a)], quasi-periodic in all directions [panel (c)], or periodic in one direction while quasi-periodic in others [panel (b)].

moiré crystals: What mechanisms drive these diverse moiré patterns, and can these quasi-periodic patterns lead to wave-function localization? To address these questions, we formulate a low-energy effective theory for small-angle rotations about a fixed axis, building upon Bistritzer and MacDonald's work [1]. Our theoretical framework elucidates the emergence of quasi-periodic moiré patterns and provides a method for classifying different types of moiré patterns based on the arithmetic property of $\boldsymbol{L}$. Through numerical analysis, we demonstrate the potential for distinct dimensional localizations within quasi-moiré crystals with different rotation axes. Recent work has identified low-dimensional compact states in incommensurate 3D moiré lattices under general three-dimensional rotations [39]. In contrast, the present work focuses on the universal low-energy moiré physics in the small-angle regime and develops an analytical continuum framework connecting the rotation axis to the moiré geometry and dimensional localization. The two studies are therefore complementary.

Model

We consider the following Hamiltonian that describes cold atoms moving in a spin-dependent lattice,

$$H = \begin{pmatrix} \dfrac{\boldsymbol{p}^2}{2m_0} + V_{\mathrm{A}} & \Omega \\ \Omega & \dfrac{\boldsymbol{p}^2}{2m_0} + V_{\mathrm{B}} \end{pmatrix}. \tag{1}$$

Here, the Hamiltonian acts on a two-component spinor wave function, whose components correspond to the two hyperfine states (spins) of an atom with mass m_0 and momentum $\boldsymbol{p}$. The atoms experience spin-dependent lattices V_{A} and V_{B}, with the two spin states coupled by an external microwave field. The coupling strength Ω is spatially uniform, indicating the field flips the spin of an atom without changing its spatial position.

We consider the case that both V_{A} and V_{B} are identical cubic lattices with a relative twist, i.e., $V_{\mathrm{A}}(\boldsymbol{r}) = V(R^{1/2}\boldsymbol{r})$ and $V_{\mathrm{B}}(\boldsymbol{r}) = V(R^{-1/2}\boldsymbol{r})$ with $V(\boldsymbol{r}) = V_0[\sin^2(\pi x) + \sin^2(\pi y) + \sin^2(\pi z)]$. Here, V_0 represents the potential depth, $R = R(\boldsymbol{L}, \theta) \in \mathrm{SO}(3)$ is the rotation matrix corresponding to axis $\boldsymbol{L}$ and angle θ, and $R^{\pm 1/2} = R(\boldsymbol{L}, \pm\theta/2)$. We assume the recoil momentum $k_{\mathrm{r}} = \pi$ for simplicity. Note that the square lattice version of Hamiltonian (1) has been recently realized in ultracold ^{87}Rb gas by the Shanxi University group [29]. Our model is a direct generalization of their experimental setup.

Low-Energy Effective Theory

In the previous work [37], we proved that the twisted lattice forms a periodic moiré crystal if and only if one can find coprime integers l_1, l_2, l_3 such that $\boldsymbol{L} = (l_1, l_2, l_3)$ and the twist angle θ satisfies $\theta = \arccos((m^2 - n^2\boldsymbol{L}^2)/(m^2 + n^2\boldsymbol{L}^2))$, for some integer $m, n \in \mathbb{Z}$. Note that all the commensurate rotations represent only a measure zero subset of SO(3), due to constraints on both rotation axis and twist angle. The incommensurate quasi-moiré crystals hence form a significantly broader parameter space compared to moiré crystals. The absence of periodicity also leads to additional complexities in numerical investigations of quasi-moiré crystals. It is thus useful to develop an effective theory that describes the system's low-energy behavior.

We rewrite the Hamiltonian as $H = H_{\rm A} + H_{\rm B} + H_{\rm AB}$, where $H_{\rm A}$ ($H_{\rm B}$) is the diagonal part that describes atoms moving in lattice $V_{\rm A}$ ($V_{\rm B}$), and $H_{\rm AB}$ is the off-diagonal coupling term. In momentum space, the diagonal Hamiltonians can be written as ($\hbar = 1$, only the lowest band is considered) $H_\sigma = \sum_{\boldsymbol{p}} \epsilon_\sigma(\boldsymbol{p})|\boldsymbol{p},\sigma\rangle\langle\boldsymbol{p},\sigma|$. Here, $|\boldsymbol{p},\sigma\rangle$ ($\sigma = {\rm A},{\rm B}$) represents the momentum $\boldsymbol{p}$ state with corresponding spin, $\epsilon_{\rm A}(\boldsymbol{p}) = \epsilon(R^{1/2}\boldsymbol{p})$ ($\epsilon_{\rm B}(\boldsymbol{p}) = \epsilon(R^{-1/2}\boldsymbol{p})$) is the dispersion for the A (B) lattice. In the tight-binding limit ($V_0 \gg E_{\rm r}$ with $E_{\rm r} = (\hbar^2\pi^2)/(2m_0)$ being the recoil energy), one has $\epsilon(\boldsymbol{p}) = -2J(\cos p_x + \cos p_y + \cos p_z)$ with J being the tunneling coefficient between nearest sites [see Supplementary Material (SM) for details].

We focus on low-energy states near the Γ point, i.e., $\boldsymbol{p} \simeq 0$. In this region, the effective-mass expansion gives

$$\epsilon_{\rm A}(\boldsymbol{p}) \simeq \epsilon_{\rm B}(\boldsymbol{p}) \simeq \frac{\boldsymbol{p}^2}{2m_{\rm eff}} - 6J, \tag{2}$$

with the effective mass $m_{\rm eff} = (2J)^{-1}$. The coupling between the two spin states is

$$\langle \boldsymbol{p},{\rm A}|H_{\rm AB}|\boldsymbol{p}',{\rm B}\rangle = 8\pi^{3/2}\Omega l_{\rm ho}^3 \sum_{\boldsymbol{G}_{\rm A},\boldsymbol{G}_{\rm B}} {\rm e}^{-(\boldsymbol{p}+\boldsymbol{G}_{\rm A})^2 l_{\rm ho}^2} \delta_{\boldsymbol{p}+\boldsymbol{G}_{\rm A},\boldsymbol{p}'+\boldsymbol{G}_{\rm B}}, \tag{3}$$

where $l_{\rm ho} = (4m_0^2 V_0 E_{\rm r})^{-1/4} \ll 1$ is the width of the Wannier function, $\boldsymbol{G}_{\rm A} \in 2\pi R^{-1/2}\mathbb{Z}^3$ ($\boldsymbol{G}_{\rm B} \in 2\pi R^{1/2}\mathbb{Z}^3$) represents the reciprocal momentum of the A (B) lattice.

Note that the coupling strength decays exponentially when $|\boldsymbol{G}_{\rm A}| \gtrsim l_{\rm ho}^{-1}$. Hence, in the spirit of Bistritzer and MacDonald [1], one concludes that when the twist angle is small such that $\theta \cdot l_{\rm ho}^{-1} \ll 1$, the $\boldsymbol{G}_{\rm B}$ terms that contribute to the summation of Eq. (3) are those that satisfy the condition $\boldsymbol{G}_{\rm B} = R\boldsymbol{G}_{\rm A}$. Under the above approximation, we can Fourier transform both Eqs. (2) and (3) to the real-space representation, which leads to an effective Hamiltonian

$$H_{\rm eff} = \frac{\boldsymbol{p}^2}{2m_{\rm eff}} + V_{\rm m}(\boldsymbol{r})\sigma_x, \tag{4}$$

with

$$V_{\rm m}(\boldsymbol{r}) = 8\pi^{3/2}\Omega l_{\rm ho}^3 \sum_{\boldsymbol{G}\in 2\pi\mathbb{Z}^3} {\rm e}^{-\boldsymbol{G}^2 l_{\rm ho}^2} {\rm e}^{{\rm i}\left(R^{\frac{1}{2}} - R^{-\frac{1}{2}}\right)\boldsymbol{G}\cdot\boldsymbol{r}}. \tag{5}$$

Utilizing the symmetry between the two spin states, we can further diagonalize $H_{\rm eff}$ by considering an even or odd combination of the two spin states. This gives a single component effective Hamiltonian $H_{{\rm eff},\pm} = (\boldsymbol{p}^2)/(2m_{\rm eff}) \pm V_{\rm m}(\boldsymbol{r})$, where $V_{\rm m}(\boldsymbol{r})$ can be viewed as an effective potential generated by the moiré pattern.

Quasi-Periodic Moiré Patterns

The structure and periodicity of a moiré pattern are closely related to the moiré potential $V_{\rm m}$, as both of them reflect the variation in local alignment (overlap) between two lattices across an extended spatial scale (in the order of θ^{-1}). Through detailed analysis of Eq. (5), we can identify several key characteristics of the moiré potential that illuminate the properties of the corresponding moiré patterns.

First, by separating the position vector $\boldsymbol{r}$ into components parallel and perpendicular to the rotation axis as $\boldsymbol{r} = \boldsymbol{r}_\parallel + \boldsymbol{r}_\perp$, it can be checked that the moiré potential $V_{\rm m}$ only depends on the perpendicular component $\boldsymbol{r}_\perp$. This observation demonstrates that the moiré pattern of a twisted 3D lattice manifests in two dimensions, thereby explaining our ability to visualize the moiré pattern in Fig. 1 through projecting 3d lattice points onto a plane perpendicular to $\boldsymbol{L}$. The property also establishes the translational invariance of $H_{\rm eff}$ along the axis $\boldsymbol{L}$, enabling the reduction of the Schrödinger equation to two dimensions and simplifying the numerical calculations.

Second, when considering a given rotation axis $\boldsymbol{L}$, the moiré potentials corresponding to different twist angles θ_1 and θ_2 exhibit a scaling relation (see SM),

$$V_{{\rm m},1}(\lambda_{\theta_1}^{-1}\boldsymbol{r}) = V_{{\rm m},2}(\lambda_{\theta_2}^{-1}\boldsymbol{r}), \tag{6}$$

where $\lambda_\theta = 2\sin(\theta/2) \simeq \theta$ represents a dimensionless scaling parameter. This relation implies that varying the twist angle θ results solely in a spatial scaling, while maintaining the basic structure of the moiré pattern.

Third, all the momentum transfers induced by the moiré potential take the form $(R^{1/2} - R^{-1/2})\boldsymbol{G}$. Since the reciprocal-lattice vectors $\boldsymbol{G}$ are spanned by $\boldsymbol{G}_1 = 2\pi(1,0,0)^{\rm T}$, $\boldsymbol{G}_2 = 2\pi(0,1,0)^{\rm T}$, and $\boldsymbol{G}_3 = 2\pi(0,0,1)^{\rm T}$, the momentum transfers induced by $V_{\rm m}$ are thus spanned by

$$\boldsymbol{q}_i = (R^{\frac{1}{2}} - R^{-\frac{1}{2}})\boldsymbol{G}_i = \lambda_\theta \frac{\boldsymbol{L}}{|\boldsymbol{L}|} \times \boldsymbol{G}_i, \quad i = 1,2,3, \tag{7}$$

which are illustrated in Fig. 1.

This observation reveals a fundamental distinction between the moiré patterns in 2D and 3D lattices, i.e., specifically in terms of the number of $\boldsymbol{q}_i$ vectors. In 2D lattices, the set of transfer momenta is generated by only two $\boldsymbol{q}_i$ vectors because $\boldsymbol{G}_i$ are the basis of a 2D reciprocal lattice. As a result, the moiré potentials (patterns) must exhibit periodicity, with their structure directly corresponding to the underlying lattice periods. This occurs because $\boldsymbol{q}_i \propto \boldsymbol{G}_i$, while the remaining coefficient and cross multiplication in Eq. (7) merely introduce a scaling and a $\pi/2$ rotation. In contrast, the 3D quasi-moiré crystals present three $\boldsymbol{q}_i$ vectors lying in the plane perpendicular to $\boldsymbol{L}$. This presents a distinctly different scenario, as they span a set $S_{\boldsymbol{q}} \equiv \{n_1\boldsymbol{q}_1 + n_2\boldsymbol{q}_2 + n_3\boldsymbol{q}_3 | n_i \in \mathbb{Z}\}$ that does not necessarily constitute a 2D Bravais (reciprocal) lattice. In the SM, we prove that all the moiré patterns can be categorized into three types, based on the arithmetic properties of $\boldsymbol{L}$. In fact, one can consider the following equation:

$$m_1 l_1 + m_2 l_2 + m_3 l_3 = 0 \text{ with } m_1, m_2, m_3 \in \mathbb{Z}. \tag{8}$$

Assuming that the number of linearly independent solutions of the equation is $n_{\rm r}$, we have the following three scenarios.

I. The *periodic* scenario: If $n_{\rm r} = 2$, e.g., $\boldsymbol{L} = (1,1,1)$, as illustrated in Fig. 1(a), there exists a non-trivial integral combination of $\boldsymbol{q}_i$ where $\sum_i n_i\boldsymbol{q}_i = 0$. In this instance, the set $S_{\boldsymbol{q}}$ forms a 2D Bravais lattice, resulting in a periodic moiré pattern. We note that the condition $n_{\rm r} = 2$ is equivalent to that the rotation axis $\boldsymbol{L}$ is proportional to some integral vectors, which is also a necessary condition for the system to form a 3D moiré crystal [37].

II. The *hybrid* scenario: If $n_{\rm r} = 1$, there exists a finite vector $\boldsymbol{q}_0$ such that the set $S_{\boldsymbol{q}}$ becomes dense on infinite parallel lines separated by $\boldsymbol{q}_0$, with these lines oriented perpendicular to $\boldsymbol{q}_0$. In this instance, the moiré pattern is periodic along $\boldsymbol{q}_0$ with a period $2\pi/|\boldsymbol{q}_0|$ while maintaining quasi-periodicity in other directions. This scenario is exemplified by $\boldsymbol{L} = (1,\varphi,\varphi^2)$, dubbed the golden axis, where $\varphi = (\sqrt{5}+1)/2$ is the golden ratio (note that $1+\varphi-\varphi^2 = 0$), as shown in Fig. 1(b), where $\boldsymbol{q}_0 = (\boldsymbol{q}_1 + \boldsymbol{q}_2 - \boldsymbol{q}_3)/3$.

III. The *ergodic* scenario: If $n_{\rm r} = 0$, the set $S_{\boldsymbol{q}}$ becomes dense on the 2D momentum plane. The moiré pattern in this instance exhibits quasi-periodicity in all planar directions. This is exemplified by $\boldsymbol{L} = (1,\sqrt{\varphi},\varphi)$, as shown in Fig. 1(c). This axis is referred to as the Kepler axis due to its components l_1, l_2, l_3 forming the sides of a right triangle known as the Kepler triangle [40], i.e., $1+\varphi = \varphi^2$. The hybrid and ergodic scenarios therefore provide two distinct quasi-periodic settings in which dimensional localization can emerge, as we examine below.

Dimensional Localization

It is well known that quantum particles moving in a quasi-periodic potential might lead to wave function localization. While our understanding of quasi-periodic systems has primarily focused on one-dimensional models, the field of higher-dimensional quasi-periodic models remains relatively unexplored. The ergodic and the hybrid quasi-moiré crystals thus present a valuable opportunity to advance both experimental and theoretical research of novel localization transitions in two dimensions. To examine the localization characteristics of both types of moiré patterns, we conduct numerical analysis (see SM) based on the inverse participation ratio (IPR) of single-particle

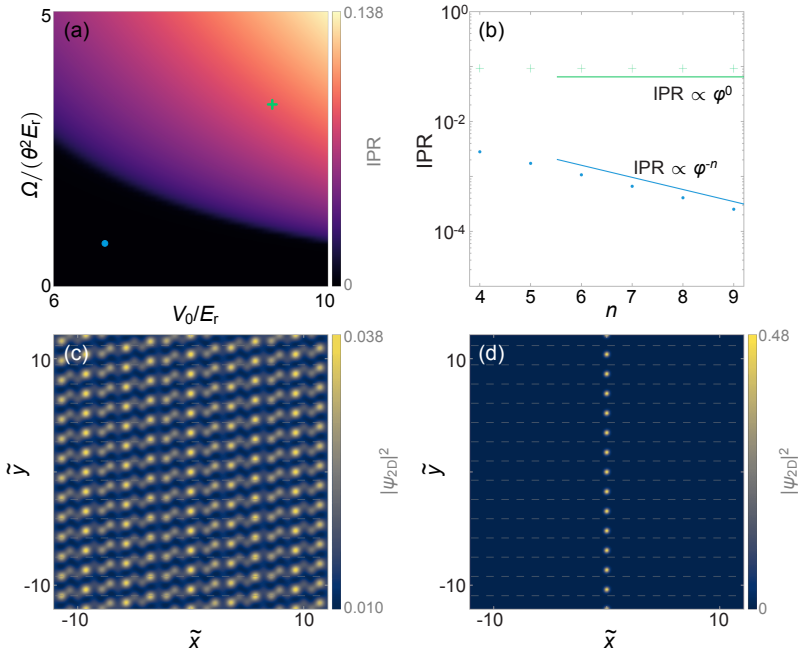

Fig. 2. Dimensional localization for quasi-moiré crystal twisted around the golden axis $\boldsymbol{L} = (1, \varphi, \varphi^2)$ (hybrid scenario). (a) The IPR as a function of potential depth V_0/E_r and normalized coupling strength $\lambda_\theta^{-2}\Omega/E_\mathrm{r} \simeq \Omega/(\theta^2 E_\mathrm{r})$. (b) The scaling of the IPR as a function of the order of the rational approximation of $\boldsymbol{L} = (1, \varphi, \varphi^2) \approx (F_n, F_{n+1}, F_{n+2})$, where F_n is the n-th Fibonacci number. (c) and (d) The 2D wave function in the plane perpendicular to $\boldsymbol{L}$. The parameters correspond to the blue [panel (c)] and green [panel (d)] dots in panel (a), respectively. $\tilde{x} = \lambda_\theta x$ and $\tilde{y} = \lambda_\theta y$ are the rescaled coordinates, where $\tilde{y}$ denotes the direction of $-\boldsymbol{q}_0$. The dashed lines mark the periodicity calculated using $\boldsymbol{q}_0$.

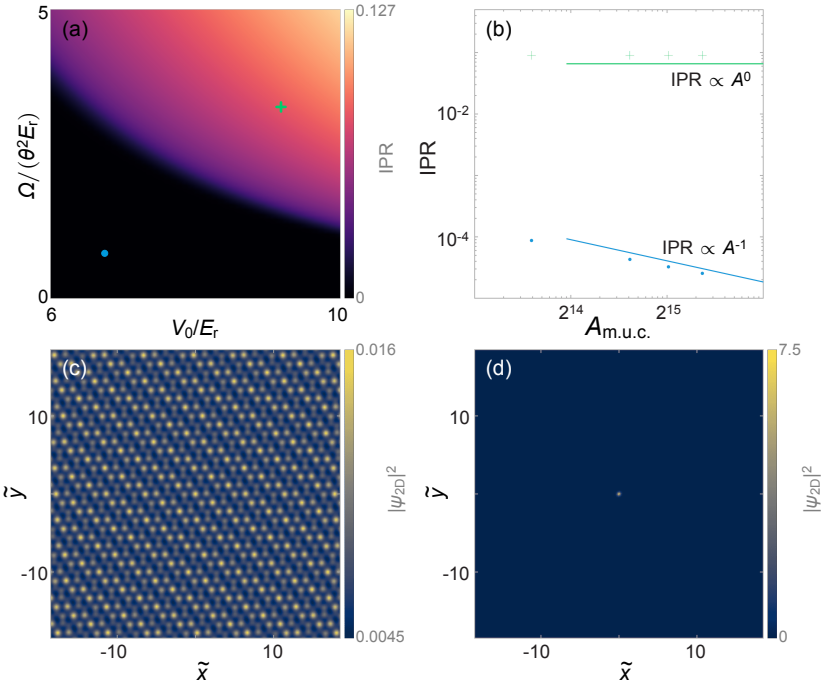

Fig. 3. Dimensional localization for quasi-moiré crystal twisted around the Kepler axis $\boldsymbol{L} = (1, \sqrt{\varphi}, \varphi)$ (ergodic scenario). (a) The IPR as a function of potential depth V_0/E_r and normalized coupling strength $\lambda_\theta^{-2}\Omega/E_\mathrm{r} \simeq \Omega/(\theta^2 E_\mathrm{r})$. (b) The scaling of the IPR as a function of $A_\mathrm{m.u.c.}$, i.e., the area of the moiré unit cell under rational approximation. (c) and (d) The 2D wave function in the plane perpendicular to $\boldsymbol{L}$. The parameters correspond to the blue [panel (c)] and green [panel (d)] dots in panel (a), respectively. $\tilde{x} = \lambda_\theta x$ and $\tilde{y} = \lambda_\theta y$ are the rescaled coordinates, where $\tilde{y}$ denotes the direction of $-\boldsymbol{q}_1$.

ground states. The IPR is defined as $\mathrm{IPR} = \int |\psi(\boldsymbol{r}_\perp)|^4 \mathrm{d}\boldsymbol{r}_\perp$ for a normalized 2D wave function $\psi(\boldsymbol{r}_\perp)$ in the plane perpendicular to $\boldsymbol{L}$, and characterizes the degree of spatial localization: a large IPR ($\sim O(1)$) indicates a state localized within a finite region, while a small IPR that scales inversely with the system area corresponds to an extended state. The dependence of localization on the twist angle follows directly from the scaling relation in Eq. (6): while θ does not alter the arithmetic classification of the moiré pattern, it enters the localization problem through the dimensionless coupling $\lambda_\theta^{-2}\Omega/E_\mathrm{r}$. Accordingly, the θ dependence of the IPR is encoded in Figs. 2(a) and 3(a); for fixed V_0 and Ω, decreasing θ increases $\lambda_\theta^{-2}\Omega/E_\mathrm{r}$ and generically favors localization.

In examining the hybrid scenario, we focus our analysis on the golden axis. Our methodology involves transforming the problem into

a periodic case by approximating the rotation axis "rationally" (see SM), i.e., $\boldsymbol{L} \simeq (F_n, F_{n+1}, F_{n+2})$ with F_n being the n-th Fibonacci number. The approximation enables us to efficiently compute the IPR of the ground state wave function within the approximate moiré unit cell. The numerical results, presented in Fig. 2(a), demonstrate a distinct transition between states where IPR $\simeq 0$ and those where IPR $= O(1)$. Figures 2(c) and 2(d) illustrate the characteristic spatial distributions of wave functions in these regions. Due to the moiré pattern's periodicity in the $\boldsymbol{q}_0$ ($\tilde{y}$) direction, the density profile in the "localized" region manifests an infinitely long line. Note that the moiré potential V_{m} is translationally invariant along the $\boldsymbol{L}$ direction. Consequently, states within the "localized" region are constrained to a 2D plane, exhibiting localization in the $\tilde{x}$ direction while maintaining extension in both the $\tilde{y}$ and $\boldsymbol{L}$ directions. We have termed this phenomenon a dimensional localized state. This dimensional localization is substantiated through analysis of the scaling of the IPRs with increasing rational approximation order n. Given that the approximate moiré unit cell period scales as φ^n in the $\tilde{x}$ direction and φ^0 in the $\tilde{y}$ direction for large n, we anticipate that the IPR of a dimensionally localized (extended) state will scale as φ^0 (φ^{-n}). This behavior has been numerically validated, as demonstrated in Fig. 2(b).

In examining the ergodic scenario, we analyze the Kepler axis. We employ an analogous rational approximation approach using Pythagorean triples to compute the IPR (see SM). Analogous to the hybrid scenario, we observe a transition between regions with IPR $\simeq 0$ and IPR $= O(1)$ in Fig. 3(a). The spatial distribution of the wave function exhibits localization characteristics in both directions perpendicular to $\boldsymbol{L}$ as illustrated in Figs. 3(c) and 3(d), attributed to the ergodic property of the moiré pattern. The transition line depicted in Fig. 3(a) thus demonstrates a dimensional localization from 3D extended states to one-dimensional confined states along the $\boldsymbol{L}$ direction. This dimensional localization is further validated through scaling analysis of the IPR as a function of the area of the moiré unit cell $A_{\mathrm{m.u.c.}}$, as presented in Fig. 3(b).

Remarks

It is worth noting that previous studies on 2D twisted lattices have also demonstrated localization transitions [13,23,30,41−49]. In periodic 2D moiré systems, localization is often associated with narrow or flat bands; by contrast, the dimensional localization reported here originates from quasi-periodicity, for which a conventional 2D Bloch-band description is unavailable in the irrational-axis limit. The surviving translational symmetries determine the extended directions: hybrid states remain extended along $\boldsymbol{q}_0$ and $\boldsymbol{L}$, whereas ergodic states remain extended only along $\boldsymbol{L}$. Although these profiles resemble non-contractible loop states [50−52] and compact localized states [53,54], those are flat-band eigenstates produced by real-space topology or destructive interference. Our states instead arise from the quasi-periodic potential and exhibit localization–delocalization transitions tunable through V_0/E_{r} and $\lambda_\theta^{-2}\Omega/E_{\mathrm{r}}$, as shown in Figs. 2 and 3.

We further clarify the distinction between the present work and Ref. [39]. Reference [39] considers a scalar potential formed by directly superimposing two cubic lattices related by a general rotation matrix. It classifies the exact 3D potential as periodic, partially periodic, or fully incommensurate and numerically identifies fully extended, plane-confined, line-confined, and fully localized states for different Euler angles. It also relates the orientation of certain confined states to the Brillouin-zone geometry of periodic approximants. By contrast, our work starts from the microscopic two-component Hamiltonian of a spin-dependent twisted optical lattice and derives a Bistritzer–MacDonald-type effective theory for the small-angle low-energy regime. The scaling relation in Eq. (6) shows that, after rescaling the spatial coordinates, the moiré geometry is independent of the twist angle, while the angle controls the overall moiré length scale and the dimensionless coupling $\lambda_\theta^{-2}\Omega/E_{\mathrm{r}}$. The momentum-transfer structure in Eq. (7) further shows that the periodicity of the effective moiré potential is governed by the integer relations among the components of the rotation axis, leading analytically to the periodic, hybrid, and ergodic classifications. These arithmetic properties determine the surviving translational symmetries and hence the directions along which the wave function remains extended. In particular, translational invariance along $\boldsymbol{L}$ excludes fully localized states within our effective theory, while permitting the plane- and line-confined states found in the hybrid and ergodic scenarios. Our results therefore complement Ref. [39] by identifying the universal small-angle mechanism underlying dimensional localization and by demonstrating localization–delocalization transitions tunable through the optical-lattice parameters.

Beyond the ground-state results discussed above, dimensional localization extends robustly into low-lying excitations, as evidenced by both IPR values and wavefunction patterns across multiple energy levels (see SM). This persistence suggests that fermionic systems may exhibit a similar effect. Furthermore, the quasi-periodic nature of the moiré potential hints at possible fractal spectral properties, with evidence derived from energy gap structures observed at sequences related to irrational parameters (e.g., Fibonacci numbers; see SM), analogous to discoveries in lower-dimensional systems including the celebrated Hofstadter butterfly [55] and similar structures in 2D moiré lattices [31,56−60]. These findings highlight the broader implications of dimensional localization and open avenues for exploring spectral and topological characteristics in 3D moiré lattices.

Experimental observation of the predicted dimensional localization may follow established wave-packet-dynamics protocols. For ultracold atoms, one may prepare a weakly interacting localized cloud, release its initial confinement in the twisted lattice, and monitor the time evolution of its density distribution [61,62]. Anisotropic arrest of expansion—along one transverse direction in the hybrid scenario and both transverse directions in the ergodic scenario, while remaining extended along $\boldsymbol{L}$—would provide a direct signature of dimensional localization. A complementary photonic realization could inject a localized probe beam into an engineered moiré lattice and infer localization from its propagation and output intensity profiles, following the protocol used to observe localization–delocalization transitions in 2D photonic moiré lattices [13].

Summary

In summary, we examine 3D moiré physics in the context of ultracold atoms confined in twisted lattices. Our findings establish that dimensionality significantly influences the low-energy physics of quasi-moiré crystals. From a geometric perspective, this influence is evidenced, within the lowest-order expansion in the angular deviation from a commensurate rotation, by the emergence of hybrid and ergodic quasi-periodic moiré patterns controlled by the arithmetic properties of the rotation axis—a mechanism absent in the corresponding 2D small-angle description. Through the development of a low-energy effective theory, we provide a comprehensive explanation for the emergence of quasi-periodicity in the moiré pattern. Numerical analysis of the effective theory demonstrates that the quasi-periodic moiré potentials can lead to novel dimensional localization transitions of atomic wave packets.

Competing interests

The authors declare no competing interests.

Author contributions

All authors contributed to the discussion of the project, the numerical calculations, and the writing of the manuscript.

Data availability

The data that support the findings of this study are available from the corresponding authors upon reasonable request.

Correspondence

Correspondence and requests for materials should be addressed to Zhe-Yu Shi or Chao Gao.

Acknowledgement

We thank Hui Zhai, Biao Lian, Jing Zhang, and Ya-Xi Shen for inspiring discussions. This work was supported by the National Natural Science Foundation of China (Grant Nos. 92576205, 12204352, 12474493, 12522413, and 12574293) and the Quantum Science and Technology–National Science and Technology Major Project (Grant No. 2025ZD0300400).

References

[1] Bistritzer R and MacDonald A H 2011 *Proc. Natl. Acad. Sci. U.S.A.* **108** 12233
[2] Cao Y, Fatemi V, Demir A, Fang S, Tomarken S L, Luo J Y, Sanchez-Yamagishi J D, Watanabe K, Taniguchi T, Kaxiras E, Ashoori R C, and Jarillo-Herrero P 2018 *Nature* **556** 80
[3] Tarnopolsky G, Kruchkov A J, and Vishwanath A 2019 *Phys. Rev. Lett.* **122** 106405
[4] Cao Y, Fatemi V, Fang S, Watanabe K, Taniguchi T, Kaxiras E, and Jarillo-Herrero P 2018 *Nature* **556** 43
[5] Wu F, MacDonald A H, and Martin I 2018 *Phys. Rev. Lett.* **121** 257001
[6] Isobe H, Yuan N F Q, and Fu L 2018 *Phys. Rev. X* **8** 041041
[7] Lian B, Wang Z, and Bernevig B A 2019 *Phys. Rev. Lett.* **122** 257002
[8] Cai J, Anderson E, Wang C, Zhang X, Liu X, Holtzmann W, Zhang Y, Fan F, Taniguchi T, Watanabe K, Ran Y, Cao T, Fu L, Xiao D, Yao W, and Xu X 2023 *Nature* **622** 63
[9] Park H, Cai J, Anderson E, Zhang Y, Zhu J, Liu X, Wang C, Holtzmann W, Hu C, Liu Z, Taniguchi T, Watanabe K, Chu J H, Cao T, Fu L, Yao W, Chang C Z, Cobden D, Xiao D, and Xu X 2023 *Nature* **622** 74
[10] Xu F, Sun Z, Jia T, Liu C, Xu C, Li C, Gu Y, Watanabe K, Taniguchi T, Tong B, Jia J, Shi Z, Jiang S, Zhang Y, Liu X, and Li T 2023 *Phys. Rev. X* **13** 031037
[11] Lu Z, Han T, Yao Y, Reddy A P, Yang J, Seo J, Watanabe K, Taniguchi T, Fu L, and Ju L 2024 *Nature* **626** 759
[12] Sunku S S, Ni G, Jiang B Y, Yoo H, Sternbach A, McLeod A S, Stauber T, Xiong L, Taniguchi T, Watanabe K, Kim P, Fogler M, and Basov D 2018 *Science* **362** 1153
[13] Wang P, Zheng Y, Chen X, Huang C, Kartashov Y V, Torner L, Konotop V V, and Ye F 2020 *Nature* **577** 42
[14] Mao X R, Shao Z K, Luan H Y, Wang S L, and Ma R M 2021 *Nat. Nanotechnol.* **16** 1099
[15] Dong K, Zhang T, Li J, Wang Q, Yang F, Rho Y, Wang D, Grigoropoulos C P, Wu J, and Yao J 2021 *Phys. Rev. Lett.* **126** 223601
[16] Lou B, Wang B, Rodríguez J A, Cappelli M, and Fan S 2022 *Sci. Adv.* **8** eadd4339
[17] Tang H, Lou B, Du F, Zhang M, Ni X, Xu W, Jin R, Fan S, and Mazur E 2023 *Sci. Adv.* **9** eadh8498
[18] Zheng Z, Sun F, Huang W, Jiang J, Zhan R, Ke Y, Chen H, and Deng S 2020 *Nano Lett.* **20** 5301
[19] Duan J, Capote-Robayna N, Taboada-Gutiérrez J, Álvarez-Pérez G, Prieto I, Martín-Sánchez J, Nikitin A Y, and Alonso-González P 2020 *Nano Lett.* **20** 5323
[20] Hu G, Ou Q, Si G, Wu Y, Wu J, Dai Z, Krasnok A, Mazor Y, Zhang Q, Bao Q, Qiu C W, and Alù A 2020 *Nature* **582** 209
[21] Chen M, Lin X, Dinh T H, Zheng Z, Shen J, Ma Q, Chen H, Jarillo-Herrero P, and Dai S 2020 *Nat. Mater.* **19** 1307
[22] Yao D, Ye L, Fu Z, Wang Q, He H, Lu J, Deng W, Huang X, Ke M, and Liu Z 2024 *Phys. Rev. Lett.* **132** 266602
[23] Ma R M, Luan H Y, Zhao Z W, Mao W Z, Wang S L, Ouyang Y H, and Shao Z K 2023 *Fundam. Res.* **3** 537
[24] Luan H Y, Ouyang Y H, Zhao Z W, Mao W Z, and Ma R M 2023 *Nature* **624** 282
[25] Spencer L, Coste N, Ni X, Park S, Schaeper O C, Kim Y D, Taniguchi T, Watanabe K, Toth M, Zalogina A, Tang H, and Aharonovichs I 2025 arXiv: 2502.09839 [physics.optics]
[26] González-Tudela A and Cirac J I 2019 *Phys. Rev. A* **100** 053604
[27] Salamon T, Celi A, Chhajlany R W, Frérot I, Lewenstein M, Tarruell L, and Rakshit D 2020 *Phys. Rev. Lett.* **125** 030504
[28] Luo X W and Zhang C 2021 *Phys. Rev. Lett.* **126** 103201
[29] Meng Z, Wang L, Han W, Liu F, Wen K, Gao C, Wang P, Chin C, and Zhang J 2023 *Nature* **615** 231
[30] Paul G C, Recher P, and Santos L 2023 *Phys. Rev. A* **108** 053305
[31] Wan X T, Gao C, and Shi Z Y 2024 arXiv: 2404.08211 [cond-mat.mes-hall]
[32] Zeng J H, Zhu Q, and He L 2025 *Phys. Rev. A* **111** 063317
[33] Tian R, Zhang Y, Wu T, Liu M, Zhang Y C, Li S, and Liu B 2024 arXiv:2407.21466 [cond-mat.quant-gas]
[34] Li T T, Guo Z H, Wang X N, and Zhu Q 2025 *Front. Phys.* **20** 042201
[35] Fang P, Gao C, and Lin J 2025 *Chaos Solitons Fractals* **195** 116314
[36] Arkhipova A A, Kartashov Y V, Ivanov S K, Zhuravitskii S A, Skryabin N N, Dyakonov I V, Kalinkin A A, Kulik S P, Kompanets V O, Chekalin S V, Ye F, Konotop V V, Torner L, and Zadkov V N 2023 *Phys. Rev. Lett.* **130** 083801
[37] Wang C, Gao C, Zhang J, Zhai H, and Shi Z Y 2024 *Phys. Rev. Lett.* **133** 163401
[38] Jin F, Ren J, Zanotti S, Cui P, Zheng H, Liang J, Ni J, Wang Z, Shi F, Qiu C W, Chang G, Liew T, and Su R 2025 *Sci. Adv.* **11** eadx2361
[39] Gao Z, Konotop V V, Peng R, Xu Z, Yang Z, and Ye F 2025 *Nat. Commun.* **16** 6306
[40] See https://en.wikipedia.org/wiki/Kepler triangle for an introduction to the geometric and arithmetic properties of Kepler triangle.
[41] Huang C, Ye F, Chen X, Kartashov Y V, Konotop V V, and Torner L 2016 *Sci. Rep.* **6** 32546
[42] Huang B and Liu W V 2019 *Phys. Rev. B* **100** 144202
[43] Moon P, Koshino M, and Son Y W 2019 *Phys. Rev. B* **99** 165430
[44] Park M J, Kim H S, and Lee S 2019 *Phys. Rev. B* **99** 245401
[45] Tang H, Du F, Carr S, DeVault C, Mello O, and Mazur E 2021 *Light Sci. Appl.* **10** 157
[46] Gonçalves M, Olyaei H Z, Amorim B, Mondaini R, Ribeiro P, and Castro E V 2021 *2D Mater.* **9** 011001
[47] Gao Z, Xu Z, Yang Z, and Ye F 2023 *Phys. Rev. A* **108** 013513
[48] Paul N, Crowley P J D, and Fu L 2024 *Phys. Rev. Lett.* **132** 246402
[49] Madroñero C, Domínguez-Castro G A, and Paredes R 2025 *Ann. Phys.* **537** 2400309
[50] Xia S, Ramachandran A, Xia S, Li D, Liu X, Tang L, Hu Y, Song D, Xu J, Leykam D, Flach S, and Chen Z 2018 *Phys. Rev. Lett.* **121** 263902
[51] Ma J, Rhim J W, Tang L, Xia S, Wang H, Zheng X, Xia S, Song D, Hu Y, Li Y, Yang B J, Leykam D, and Chen Z 2020 *Phys. Rev. Lett.* **124** 183901
[52] Song L, Xie Y, Xia S, Tang L, Song D, Rhim J W, and Chen Z 2023 *Laser Photonics Rev.* **17** 2200315
[53] Vicencio R A, Cantillano C, Morales-Inostroza L, Real B, Mejía-Cortés C, Weimann S, Szameit A, and Molina M I 2015 *Phys. Rev. Lett.* **114** 245503
[54] Mukherjee S, Spracklen A, Choudhury D, Goldman N, Öhberg P, Andersson E, and Thomson R R 2015 *Phys. Rev. Lett.* **114** 245504
[55] Hofstadter D R 1976 *Phys. Rev. B* **14** 2239
[56] Bistritzer R and MacDonald A H 2011 *Phys. Rev. B* **84** 035440
[57] Dean C R, Wang L, Maher P, Forsythe C, Ghahari F, Gao Y, Katoch J, Ishigami M, Moon P, Koshino M, Taniguchi T, Watanabe K, Shepard K L, Hone J, and Kim P 2013 *Nature* **497** 598
[58] Ponomarenko L A, Gorbachev R V, Yu G L, Elias D C, Jalil R, Patel A A, Mishchenko A, Mayorov A S, Woods C R, Wallbank J R, Mucha-Kruczynski M, Piot B A, Potemski M, Grigorieva I V, Novoselov K S, Guinea F, Fal'ko V I, and Geim A K 2013 *Nature* **497** 594
[59] Hunt B, Sanchez-Yamagishi J D, Young A F, Yankowitz M, LeRoy B J, Watanabe K, Taniguchi T, Moon P, Koshino M, Jarillo-Herrero P, and Ashoori R C 2013 *Science* **340** 1427
[60] Lu X, Lian B, Chaudhary G *et al.* 2021 *Proc. Natl. Acad. Sci. U.S.A.* **118** e2100006118
[61] Roati G, D'Errico C, Fallani L, Fattori M, Fort C, Zaccanti M, Modugno G, Modugno M, and Inguscio M 2008 *Nature* **453** 895
[62] Billy J, Josse V, Zuo Z, Bernard A, Hambrecht B, Lugan P, Clément D, Sanchez-Palencia L, Bouyer P, and Aspect A 2008 *Nature* **453** 891